

Optically Transparent Lead Halide Perovskite Polycrystalline Ceramics

Michael C. Brennan,* Christopher L. McCleese, Lauren M. Loftus, Jeremiah Lipp, Michael Febbraro, Harris J. Hall, David B. Turner, Michael J. Carter, Peter R. Stevenson, and Tod A. Grusenmeyer*



Cite This: <https://doi.org/10.1021/acsami.4c01517>



Read Online

ACCESS |



Metrics & More



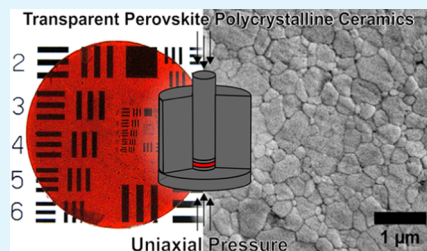
Article Recommendations



Supporting Information

ABSTRACT: We utilize room-temperature uniaxial pressing at applied loads achievable with low-cost, laboratory-scale presses to fabricate freestanding $\text{CH}_3\text{NH}_3\text{PbX}_3$ ($\text{X}^- = \text{Br}^-, \text{Cl}^-$) polycrystalline ceramics with millimeter thicknesses and optical transparency up to ~70% in the infrared. As-fabricated perovskite ceramics can be produced with desirable form factors (i.e., size, shape, and thickness) and high-quality surfaces without any postprocessing (e.g., cutting or polishing). This method should be broadly applicable to a large swath of metal halide perovskites, not just the compositions shown here. In addition to fabrication, we analyze microstructure–optical property relationships through detailed experiments (e.g., transmission measurements, electron microscopy, X-ray tomography, optical profilometry, etc.) as well as modeling based on Mie theory. The optical, electrical, and mechanical properties of perovskite polycrystalline ceramics are benchmarked against those of single-crystalline analogues through spectroscopic ellipsometry, Hall measurements, and nanoindentation. Finally, γ -ray scintillation from a transparent MAPbBr_3 ceramic is demonstrated under irradiation from a ^{137}Cs source. From a broader perspective, scalable methods to produce freestanding polycrystalline lead halide perovskites with comparable properties to their single-crystal counterparts could enable key advancements in the commercial production of perovskite-based technologies (e.g., direct X-ray/ γ -ray detectors, scintillators, and nonlinear optics).

KEYWORDS: transparent ceramics, uniaxial press, lead halide perovskites, scintillators, polycrystalline wafer, optical transparency, light scattering theory



INTRODUCTION

Inexpensive starting materials, low-temperature synthesis, and readily tailored optical properties have motivated the use of lead halide perovskites (APbX_3 ; $\text{A}^+ = \text{CH}_3\text{NH}_3^+$ [MA^+], $\text{CH}(\text{NH}_2)_2^+$ [FA^+], Cs^+ ; $\text{X}^- = \text{I}^-, \text{Br}^-, \text{Cl}^-$) in a broad range of applications. These include solar cells,¹ direct X-ray/ γ -ray detectors,^{2–4} scintillators,^{2–5} light-emitting diodes,⁵ lasers,^{6,7} nonlinear optics,⁸ and visible/infrared photodetectors.^{9,10} Many target applications require thick (≥ 1 mm) optical components with complex form factors (i.e., size, shape, and thickness) as well as high broadband optical transparency in the visible to infrared wavelength regimes. Single crystals are ideal in such applications, as their lack of grain boundaries, pores, and secondary phases leads to enhanced optical transparency. However, single crystals grown by melt-based approaches (e.g., Bridgman) are limited to all-inorganic perovskites due to organic cation volatility, and solution-based methods are inundated with reproducibility and scalability issues. Moreover, postprocessing (e.g., cutting and polishing) to achieve application-specific physical dimensions and surface quality is challenging for these soft^{11,12} ionic materials. On the other hand, perovskite thin-film fabrication techniques cannot easily reach thicknesses $\gg 1$ μm while maintaining high-quality morphology (e.g., minimal pin-holes).

Thus, demand exists for reliable material processing routes to produce form factor-flexible, optically transparent lead halide perovskites.

Transparent oxide and II–VI polycrystalline ceramics (e.g., $\text{Y}_3\text{Al}_5\text{O}_{12}$ [YAG], Y_2O_3 , Al_2O_3 , ZrO_2 , MgO , MgAl_2O_4 , ZnO , ZnS , and ZnSe) have replaced their single-crystal counterparts in many applications (e.g., optical lenses, radar domes, transparent armor, solid-state lasers, scintillators, etc.).^{13–17} This transition has been linked in large part to better scalability of ceramic versus single-crystal processing techniques. However, fabricating transparent oxide and II–VI ceramics often requires a combination of expensive, specialized sintering equipment, such as hot isostatic presses, spark plasma/field-assisted sintering technologies, vacuum sintering chambers, or dynamic chemical vapor deposition chambers. This dedicated equipment is necessary to achieve the requisite temperatures (>700 °C) and pressures (~ 10 to ~ 100 s of MPa) necessary to

Received: January 26, 2024

Revised: February 27, 2024

Accepted: March 1, 2024

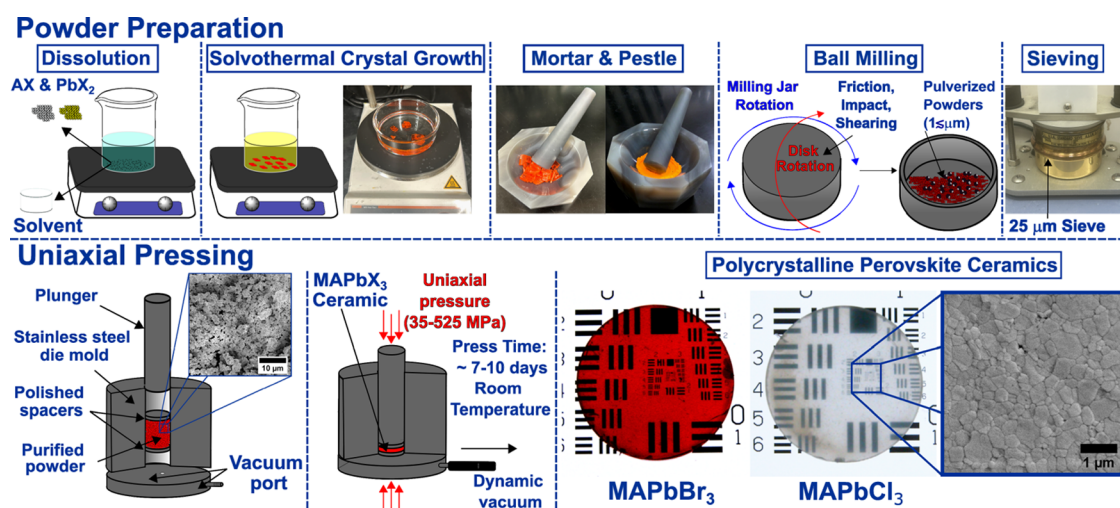


Figure 1. Processing guidelines for the production of transparent MAPbX_3 ($X = \text{Br}^-$, Cl^-) ceramics.

transform porous green body compacts or vapor phase reactants into dense white body ceramics. In stark contrast, the soft ionic bonding nature of the lead halide perovskite framework permits pressure-induced mass transport processes at significantly lower temperatures ($<100^\circ\text{C}$).¹⁸ Thus, dense halide perovskite ceramics can be fabricated via widely available low-temperature uniaxial pressing methods.

Immediate examples are works by Shrestha et al.¹⁹ and Deumel et al.²⁰ demonstrating ~ 13 mm diameter by ~ 1 mm thick MAPbI_3 polycrystalline ceramics with relative densities (ρ)—defined as the polycrystalline ceramic's density divided by the material's theoretical maximum density—of $\rho \gtrsim 0.90$. Interestingly, these ceramics were formed at room temperature, requiring only ~ 5 to ~ 30 min of uniaxial pressing of solution-made powders at ~ 75 to ~ 300 MPa.¹⁹ The ability to rapidly produce MAPbI_3 ceramics has been linked to plastic deformation based on nanoindentation measurements.^{19,21} Lead halide perovskite ceramic-based direct X-ray detectors demonstrated conversion efficiencies that are superior to MAPbI_3 thin-film-based detectors.²² These polycrystalline ceramic-based X-ray detectors are also comparable to single-crystalline MAPbI_3 ²³ detectors as well as state-of-the-art CdTe-based detectors, illustrating utility beyond academic interests.^{19,20,33}

In tandem, facile fabrication methods and demonstrated radiation detection capabilities have motivated intriguing, recent research into ceramic processing of metal halides e.g., MAPbI_3 ,^{19–27} MAPbBr_3 ,²⁴ MAPbCl_3 ,²⁶ CsPbBr_3 ,^{28,29} CsSnI_3 ,^{26,30} $\text{CsSn}(\text{Br}_{0.5}\text{Cl}_{0.5})_3$,³¹ $\text{Cs}_2\text{AgBiBr}_6$,³² $(\text{CH}_3\text{NH}_3)_3\text{BiI}_9$,^{26,33} and $[(\text{C}_6\text{H}_5)_3\text{P}]_2\text{MnBr}_4$.³⁴ Despite increasing research on this topic, freestanding ~ 1 mm thick halide perovskite ceramics with high optical transparency have yet to be demonstrated. Lack of transparency to visible and infrared light stymies the potential integration of perovskite ceramics in a number of applications. Moreover, high optical transparency itself signifies high density, minimal pores, and a lack of impurities and secondary phases at grain boundaries. These characteristics should lead to better perovskite semiconducting properties^{35,36} as well as improved mechanical durability.³⁷ Thus, optically transparent perovskite ceramics may not only demonstrate enhanced performance in direct X-ray/ γ -ray detectors but also have potential utility as nonlinear

optical components, scintillators, or rare-earth doped solid-state lasers.

In this work, we outline material processing methods to produce MAPbBr_3 and MAPbCl_3 ceramics with areas of ~ 125 mm^2 and thicknesses (l) between ~ 0.5 and ~ 1.9 mm. MAPbX_3 ceramics demonstrate optical transparency $\gtrsim 70\%$ of their theoretical maximum transmission in the near- and short-wave infrared (~ 800 to ~ 2000 nm). We benchmark the optoelectronic and mechanical properties of the freestanding polycrystalline perovskites against single-crystalline analogues. Finally, we show evidence of γ -ray scintillation from the transparent perovskite ceramics, highlighting a potential application for the materials discussed in this work. Overall, the data demonstrate that microstructural properties (e.g., crystal structure, average grain size ($\langle d_g \rangle$), root-mean-squared surface roughness (S_q), ρ , composition, pores, etc.) can be controlled in order to develop lead halide perovskite ceramics with optical properties tailored to meet the performance metrics of specific applications.

RESULTS AND DISCUSSION

Optical Transparency in Polycrystalline Ceramics.

Thick polycrystalline ceramics can be defined as transparent, translucent, or opaque. The term “transparent” should largely be reserved for materials having transmission $\gtrsim 70\%$ of their theoretical maximum transmission (accounting for reflection losses) in the wavelength range of interest.^{38–44} In hundreds of microns to millimeter-thick semiconducting materials, optical transparency occurs at wavelengths with sufficiently low absorption coefficients (i.e., $\alpha < 1$). MAPbBr_3 and MAPbCl_3 have optical bandgaps (E_g) of ~ 535 and ~ 405 nm, respectively. At shorter wavelengths ($\lambda \lesssim E_g$), α is on the order of $\sim 10^5$ to 10^6 cm^{-1} .^{45–49} Furthermore, strong vibrational absorption from the organic CH_3NH_3^+ moieties occurs when $\lambda \gtrsim 2100$ nm (see Figure S1). At wavelengths between the optical bandgaps and vibrational absorption, a transmission window exists where $\alpha \lesssim 10^{-1}$ cm^{-1} .^{45–50} Therefore, we focus our transparency discussion on the wavelength regime from the MAPbBr_3 and MAPbCl_3 optical bandgaps up to ~ 2000 nm. However, we show other transparency windows at longer wavelengths as well.

Achieving high optical transparency in thick polycrystalline materials requires stringent control over microstructural

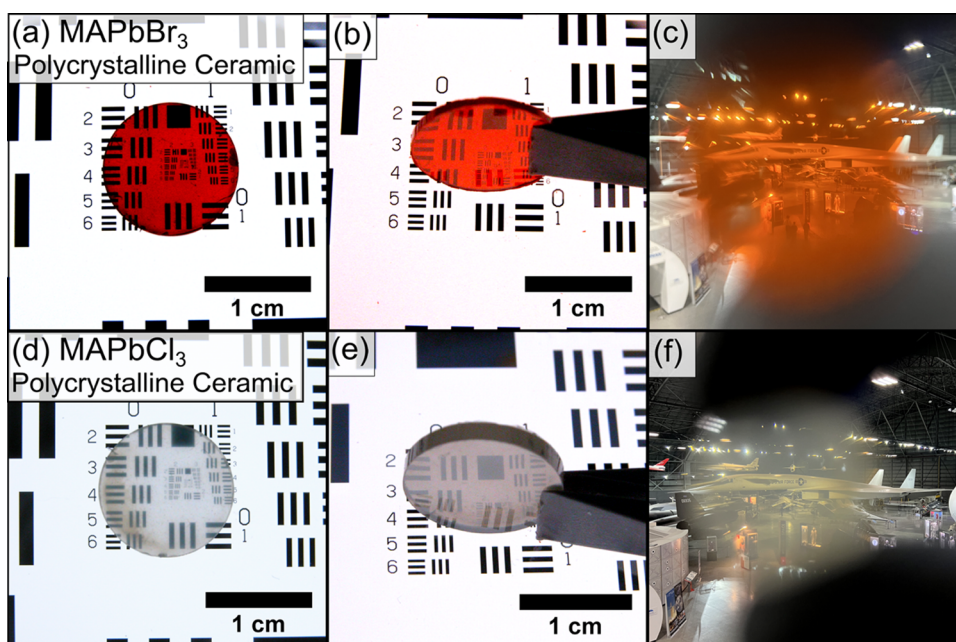


Figure 2. Representative images of $l = 0.989$ mm MAPbBr₃ (a–c) and $l = 1.874$ mm MAPbCl₃ (d–f) ceramics (diameters of ~ 12.7 mm). This includes both straight-on (a, d) and side (b, e) views of each ceramic on a USAF 1951 test target as well as images through each ceramic (c, f) of an XB-70 Valkyrie at the National Museum of the USAF from ~ 50 m away (for reference, the Valkyrie is ~ 56 m in length and ~ 10 m tall).

properties to reduce undesired scattering at the surface or within the ceramic. Significant scattering sources in polycrystalline materials include: (i) optical anisotropy between grains, (ii) impurities or secondary phases typically existing at grain boundaries, (iii) high surface roughness ($\gg \lambda/10$), and (iv) pores.^{13–18,38–43} In order to obtain high optical transparency, each scattering source must be reduced or eliminated. Throughout the remaining discussion, we will highlight how each scattering source is minimized and analyze the implication of microstructure on the ceramics' transparency.

Fabricating Optically Transparent Lead Halide Perovskite Ceramics. With the goal of high optical transparency, material selection is the first critical consideration. Here, MAPbBr₃ and MAPbCl₃ have been chosen for two important reasons. (i) Each composition adopts cubic crystal symmetry at room temperature (see X-ray diffraction [XRD] patterns in Figure S2 along with measurement details in the Supporting Information [SI]), and (ii) mature synthetic methods for high-purity single crystals exist for each composition.^{51,52} Both are critical toward eliminating scattering sources within the final ceramic.

First, cubic symmetry eliminates scattering linked to optical anisotropy at grain boundaries.^{40,41} Second, single-crystal source materials—as opposed to solution-processed or mechanochemically produced microcrystalline/nanocrystalline powders—are advantageous due to their higher purity and more perfect stoichiometry.²⁷ Both minimize scattering linked to the presence of secondary phases or impurities in the final ceramic. The high chemical purity of prepressed powders is supported by XRD measurements (Figure S2) and thermogravimetric analysis (Figure S3), which show only perovskite-linked Bragg reflections and mass loss consistent with only CH₃NH₃X and PbX₂ decomposition.⁵³

Figure 1 outlines the processing guidelines employed to produce transparent MAPbX₃ ($X^- = \text{Br}^-, \text{Cl}^-$) ceramics. Millimeter to centimeter-sized bulk MAPbX₃ crystals were first

grown via modified solvothermal methods (see the SI for crystal growth and purification details).⁵¹ Two subsequent pulverization steps with a planetary ball mill followed the solvothermal crystal growth. The only difference between these two steps was the diameter of the zirconia milling media (15 mm balls in the first step and 2 mm balls in the second step). See the SI for further ball milling details. Finally, powders were sieved through 125 μm and then 25 μm mesh to remove excessively large grains. The end results were irregularly shaped grains with sizes ranging from <100 nm to several microns based on scanning electron microscopy (SEM) analysis (see Figure S4 and SEM method details in the SI).

Pulverized and sieved powders were then loaded into evacuable stainless steel die sets (~ 12.7 mm diameters) sandwiched between two polished stainless steel spacer pellets and placed onto uniaxial presses. Die sets with perovskite powders were dried under vacuum for ca. 1–2 h prior to application of pressure. Three pressure stages were applied under a dynamic vacuum at room temperature ($\sim 21 \pm 2$ °C). The first two lower-pressure stages (35 MPa for ~ 1 h and 150 MPa for ~ 2 h) were used to produce an opaque green body compact (see Figure S5). Then, select finishing stage pressures between ~ 200 and ~ 525 MPa were set for ~ 150 to ~ 300 h. Finishing stage pressures and press times depend on the thickness of the ceramic (see the SI for further uniaxial pressing details). Finally, the perovskite ceramics were carefully removed from the die sets. All ceramics were characterized thereafter without any additional annealing or polishing steps.

Optically Transparent MAPbX₃ Perovskite Ceramics. Figure 2a–f shows representative images of MAPbBr₃ and MAPbCl₃ ceramics with diameters of 12.7 mm produced using the methods outlined above. Figure 2a,d displays backlit ceramics laid flat on an Edmund Optics fused silica United States Air Force (USAF) 1951 test target. Figure 2b,e portrays side views of the same ceramics to illustrate thicknesses of $l = 0.989$ mm (MAPbBr₃) and $l = 1.874$ mm (MAPbCl₃). Figure

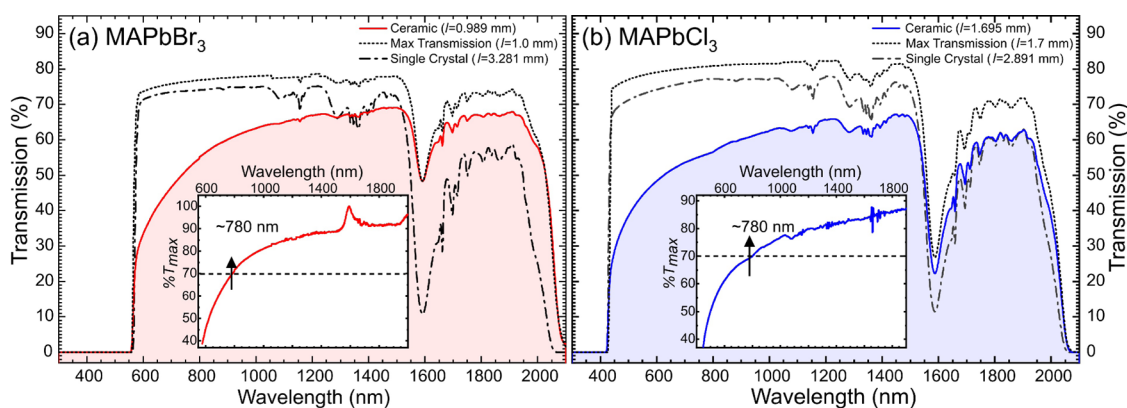


Figure 3. Transmission spectra from 300 to 2100 nm of $l = 0.989$ mm MAPbBr₃ (a) and $l = 1.695$ mm MAPbCl₃ (b) ceramics (solid lines/shaded regions). Corresponding theoretical maximum (black dotted lines) and single-crystal (black dashed-dotted lines) spectra are provided. Insets: percent of perovskite theoretical max transmission for each ceramic (i.e., red or blue line divided by dashed black lines in each plot).

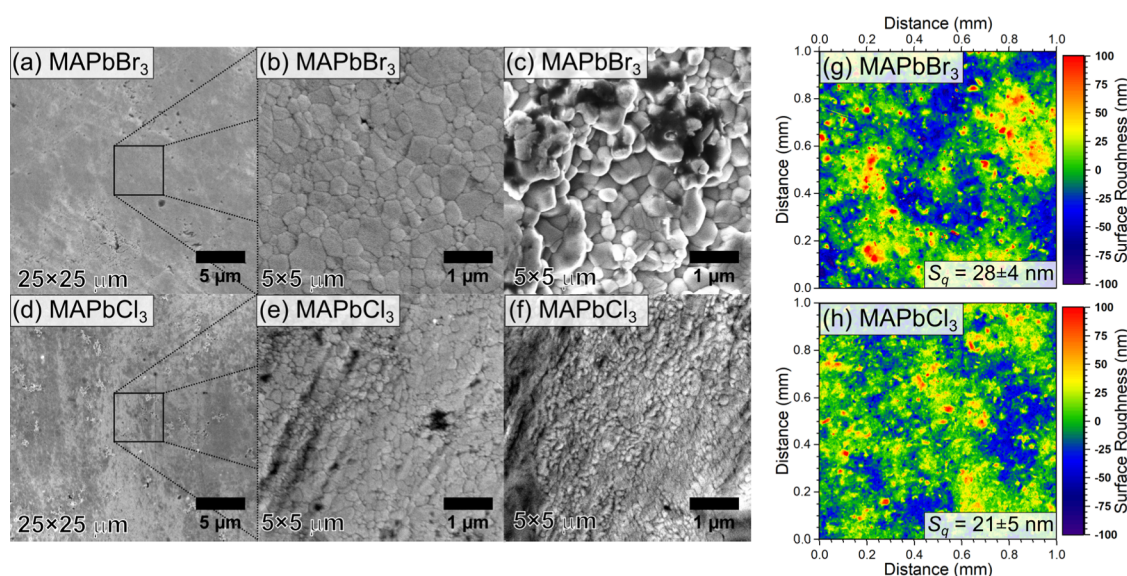


Figure 4. SEM micrographs of $l = 0.989$ mm MAPbBr₃ (a–c) and $l = 1.695$ mm MAPbCl₃ (d–f) ceramics. This includes images of $25 \mu\text{m} \times 25 \mu\text{m}$ (a, d) and $5 \mu\text{m} \times 5 \mu\text{m}$ areas of ceramic surfaces (b, e) as well as $5 \mu\text{m} \times 5 \mu\text{m}$ areas of ceramic cross sections (c, f). Surface roughness maps for $1 \text{ mm} \times 1 \text{ mm}$ areas of each ceramic are provided for MAPbBr₃ (g) and MAPbCl₃ (h). Root-mean-squared surface roughness (S_q) values are given at the bottom right of each roughness map.

2c,f depicts images through each ceramic of an XB-70 Valkyrie (North American Aviation Company) at the National Museum of the USAF. Figures S6 and S7 show test target images of several other MAPbBr₃ and MAPbCl₃ ceramics with various thicknesses ($0.5 \lesssim l \lesssim 1.9$ mm), demonstrating form factor flexibility. Details of imaging conditions can be found in the SI.

Transmission measurements were performed with a Cary 5000 UV–Vis–NIR spectrophotometer. Metal plates with $\varnothing \sim 4$ mm apertures were placed in the light path between the sample and detector to limit forward scattering from being quantified as transmission.⁴⁰ Figure 3a,b illustrates transmission spectra from 300 to 2100 nm of $l = 0.989$ mm MAPbBr₃ (solid red line/shaded region) and $l = 1.695$ mm MAPbCl₃ (solid blue line/shaded region) ceramics. The black dotted and dashed-dotted lines represent the corresponding theoretical maximum and single-crystal transmission spectra, respectively. Figure S8 shows pictures of solution-grown MAPbX₃ single crystals used in transmission measurements. The insets of Figure 3a,b plot the percent of each perovskite's theoretical max transmission ($\%T_{\text{max}}$) for each ceramic, which

was derived by dividing the theory (dashed lines) into experiment (colored lines) over the wavelength range of interest. The insets demonstrate how close each ceramic is to its theoretical maximum and should not be confused with raw transmission values, as measured by the spectrophotometer. Transmission data demonstrates that each ceramic achieves $\geq 70\%$ of the theoretical maximum transmission for each perovskite composition from ~ 780 to ~ 2000 nm. The dip in transmission at ~ 1590 nm is linked to weak CH_3NH_3^+ vibrational overtone absorption. Spectra for replicate MAPbBr₃ and MAPbCl₃ ceramics are provided in Figure S9. Perovskite ceramics maintain between ~ 70 and 98% of their initial transparency in the ~ 780 and 2000 nm transmission window for at least ~ 9 months after synthesis (see Figure S10).

Of further interest is perovskite ceramics' transmission at longer wavelengths. Figure S11 plots transmission spectra from 0.3 to $25 \mu\text{m}$ for the $l = 0.989$ mm MAPbBr₃ ceramic along with other commercially available transparent polycrystalline ceramics—ZnSe, ZnS, Al₂O₃, and YAG—for comparison. While CH_3NH_3^+ vibrational absorption is prevalent through-

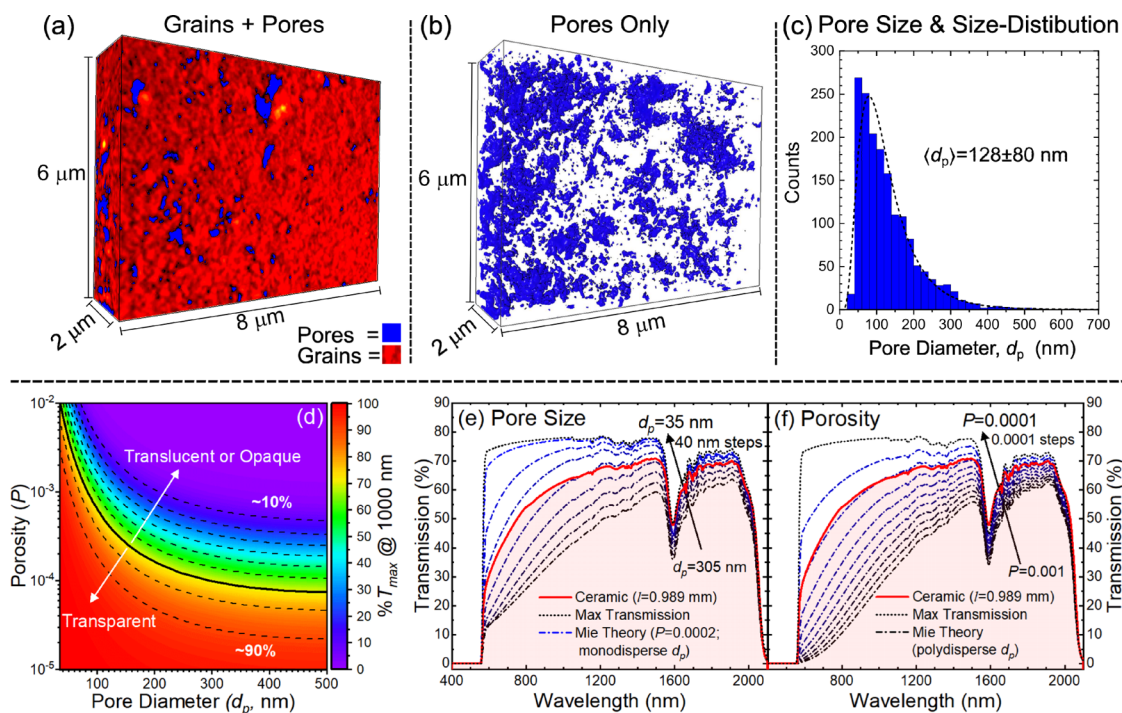


Figure 5. NanoCT analysis of an $8 \mu\text{m} \times 6 \mu\text{m} \times 2 \mu\text{m}$ region of the $l = 0.989 \text{ mm}$ MAPbBr₃ ceramic. (a) An overlay of grains (red shaded regions) and pores (blue shaded regions) and (b) a view of only pores in the same area. (c) Histogram of pore diameters from NanoCT scans (~ 1600 pores sampled with a 20 nm bin size). Average pore size ($\langle d_p \rangle$) and size distribution are provided. (d) A contour plot that models $\%T_{\text{max}}$ at 1000 nm as a function of monodisperse pore size and porosity for an $l \sim 1 \text{ mm}$ MAPbBr₃ ceramic. The dashed black lines trace $\%T_{\text{max}}$ in 10% steps from ~ 10 to 90%. Transmission spectra modeled via Mie theory (dashed-dotted black/blue lines) as a function of (e) pore diameter (35 nm $< d_p <$ 305 nm; 40 nm steps; monodisperse d_p ; $P = 0.0002$) and (f) porosity (0.001 $< P <$ 0.0001; 0.0001 steps; polydisperse d_p). Experimental transmission spectra of $l = 0.989 \text{ mm}$ MAPbBr₃ (red line/shaded region) and the corresponding maximum theoretical transmission (dotted black line) are provided in (e) and (f).

out the infrared, high transparency windows are observed from ~ 2.5 to $\sim 3.0 \mu\text{m}$, from ~ 4.2 to $\sim 5.2 \mu\text{m}$, and from ~ 12 to $\sim 20 \mu\text{m}$. Such windows may make lead halide perovskite ceramics appealing host materials for rare-earth dopants in perovskite ceramic-based solid-state infrared lasers.⁷ Details on the transmission of all measurements and max transmission calculations can be found in the SI.

Optically Transparent MAPbX₃ Perovskite Ceramic Microstructures: Grain Size and Surface Roughness. To the best of our knowledge, the transmission data in Figures 3 and S9 demonstrate the highest optical transparency reported to date for any halide perovskite polycrystalline ceramics ($0.5 \lesssim l \lesssim 2 \text{ mm}$) produced via uniaxial pressing. Transmission values also approach the theoretical maximum and are comparable to single crystals, making perovskite ceramics viable candidates to replace single crystals in several applications. Still, there is clearly room for improvement, with respect to pressed powder transmission. Attaining near theoretical maximum transmission through perovskite ceramics will first require insight into what is causing the remaining scattering. For this, we turn to a detailed analysis of MAPbX₃ ceramic microstructural properties.

Figure 4 shows SEM images of $l = 0.989 \text{ mm}$ MAPbBr₃ (Figure 4a–c) and $l = 1.695 \text{ mm}$ MAPbCl₃ (Figure 4d–f) ceramics. SEM methods and analysis details can be found in the SI. Representative $25 \mu\text{m} \times 25 \mu\text{m}$ area images of ceramic surfaces are given in Figure 4a,d. Magnified $5 \mu\text{m} \times 5 \mu\text{m}$ SEM images are shown in Figure 4b,e (surface images) and Figure 4c,f (cross-sectional images). In both the $5 \mu\text{m} \times 5 \mu\text{m}$ surface and cross-sectional SEM micrographs, individual grains can be

resolved. Apparent average grain sizes estimated from surface SEM images are $\langle d_g \rangle = 338 \pm 194 \text{ nm}$ (MAPbBr₃) and $\langle d_g \rangle = 212 \pm 82 \text{ nm}$ (MAPbCl₃) with relatively large size distributions (see grain size histograms in Figure S12). Table S1 lists surface-derived $\langle d_g \rangle$ values, along with other details, for all ceramics in this work.

To further examine surface quality, optical profilometry measurements in Figure 4g,h illustrate representative surface roughness maps over $1 \text{ mm} \times 1 \text{ mm}$ areas for $l = 0.989 \text{ mm}$ MAPbBr₃ and $l = 1.695 \text{ mm}$ MAPbCl₃ ceramics (see the SI for further profilometry methods). Root-mean-squared surface roughness values are averaged from three separate $1 \text{ mm} \times 1 \text{ mm}$ maps. Values range from $S_q \sim 20$ to $\sim 30 \text{ nm}$ for all ceramics and are significantly smaller than the ~ 550 to 2000 nm wavelength range of interest ($\lambda/100 \lesssim S_q \lesssim \lambda/20$). Peak-to-valley roughness variations are on the order of $\sim 200 \text{ nm}$, which may lead to enhanced scatter at shorter wavelengths (near the band edge). However, it is worth noting that the variations occur laterally over distances of ca. 50 – $100 \mu\text{m}$. This corresponds to local surface tilting $< 1^\circ$, leading to marginally increased diffuse reflectance. Overall, the surface roughness should have minimal contribution to transmission losses observed in Figure 3.^{38–44} Table S1 also lists S_q and the corresponding standard deviations for all ceramics.

Interestingly, perovskite S_q values reflect that of the polished stainless steel spacers ($S_q \sim 15 \text{ nm}$) that are in contact with the perovskite ceramic surfaces during uniaxial pressing (see Figure S13). This surface mirroring effect is likely due to the plastic deformation of MAPbX₃ perovskite grains, causing them to conform to much harder (prepolished) stainless steel spacer

surfaces during densification.^{11,12} Further improvements to perovskite surface roughness may therefore be possible by polishing spacer materials down to $S_q < 10$ nm. This would eliminate the need for postprocessing (e.g., polishing and cutting) of perovskite ceramics to attain optical grade surface quality directly out of the uniaxial press.

Optically Transparent MAPbX₃ Perovskite Ceramic Microstructures: Pores. Three of the four scattering sources described in the first section—optical anisotropy between grains, impurities/secondary phases, and surface roughness, have been minimized using our methodology. Thus, the only remaining, but undoubtedly the most significant, scattering source is residual porosity. Light scattering from pores is linked to refractive index differences between air ($n = 1$) and the polycrystalline medium ($n \approx 1.9$ and $n \approx 2.0$ between ~ 800 and ~ 2000 nm for MAPbCl₃ and MAPbBr₃, respectively).^{45–49} As will be demonstrated by the modeling below, the magnitude/efficiency of pore scattering is intertwined between pore diameter (d_p), pore size distribution, and porosity (P , the volume fraction of pores).⁴⁰ While pores can never be entirely eliminated, the ultimate goal is to minimize both porosity and pore size. It should be noted that accurate experimental quantification of porosity and pore size remains extremely challenging.^{40,54}

Porosity is ultimately linked to the ceramic density such that $P = 1 - \rho$.^{38,39} Relative densities for the perovskite ceramics—estimated from Archimedes' method (see Methods in the SI and Table S1 for more details)—range from $\rho \sim 0.973$ and ~ 0.996 , leaving residual porosities from $P \sim 0.027$ to ~ 0.004 . Unfortunately, accurate quantification of P values $\lesssim 0.01$ via Archimedes' method is not reliable using common laboratory analytical balances, and changes in P as low as ~ 0.0001 can significantly affect transmission.^{39–44} Nonetheless, Archimedes' measurements clearly demonstrate our perovskite ceramics are highly dense.

We further investigate pores using X-ray nanotomography (NanoCT) to map three-dimensional cross sections of the ceramic with a nominal spatial resolution down to ~ 50 nm and a voxel size of 16 nm. Here, the contrast between X-ray absorption (or lack thereof) by perovskite grains and pores permits determination of critical pore attributes (average pore size $\langle d_p \rangle$, size distribution, and rough morphology). Figure 5 depicts NanoCT data for an $8 \mu\text{m} \times 6 \mu\text{m} \times 2 \mu\text{m}$ region of the $l = 0.989$ mm MAPbBr₃ ceramic. Figure 5a first illustrates an overlay of the perovskite grains (red shaded regions) and pores (blue shaded region), whereas Figure 5b removes all grains and displays only pores. Video S1 shows a 3D, rotating view of this data. Figure S14 shows the entire region analyzed by NanoCT and SEM images of the ceramic fragment. NanoCT methods can be found in the SI.

Approximately 1600 pores were sampled in the analyzed area. Irregularly shaped pores are clearly observed in Figure 5a,b and Video S1. We therefore quantify average pore size and size distribution using mean Feret diameters (i.e., an average between the longest and shortest dimensions of a given pore). Figure 5c plots a histogram of mean Feret pore diameters that demonstrate $\langle d_p \rangle$ to be $\sim 128 \pm 80$ nm with a log-normal size distribution. Figure S15 shows size histograms for the minimum and maximum Feret pore diameters ($\langle d_{p,\text{min}} \rangle = 88 \pm 56$ nm; $\langle d_{p,\text{max}} \rangle = 163 \pm 105$ nm). Mean pore dimensions are between $\sim \lambda/4$ and $\sim \lambda/15$ ($\sim \lambda_{\text{eff}}/2$ and $\sim \lambda_{\text{eff}}/8$ for $n = 2$) within the MAPbBr₃ transmission window (~ 535 to ~ 2000 nm), explaining the more significant scattering effects

observed near the perovskite band edge versus longer wavelength (see Figures 3a and S9).⁴⁰

While it is clear that reducing d_p and P will enhance transparency, the exact values of each parameter necessary to optimize optical transparency for perovskite ceramics are not well understood. We thus model the effects of P and d_p on optical transparency through a combination of Mie theory⁵⁵ to estimate pore scattering efficiencies, cross sections, and extinction coefficients (see Figure S16) and Beer–Lambert extinction law to calculate transmission (see Figure S17).^{38–40} The model assumes spherical pores filled with air surrounded by a bulk material with the refractive index of MAPbBr₃.^{45–49} Full details of the modeling are provided in the SI, but we also recommend an excellent review by Hřibálová et al.⁴⁰ for a complete overview of pore scattering models.

Figure 5d first shows a contour plot that surveys the effect of both P and d_p on the percent of max transmission ($\%T_{\text{max}}$) at 1000 nm for an $l \sim 1$ mm MAPbBr₃ ceramic. The dashed lines highlight $\%T_{\text{max}}$ in 10% steps, where the solid line (and green-yellow-orange regions) indicate the $\sim 70\%$ T_{max} transparency threshold. Figure S18 shows identical contour plots at 800 and 1500 nm. These plots provide tangible microstructural requirements that are necessary to achieve near-optimal optical transparency of MAPbBr₃ ceramics at various wavelengths. To dive deeper into the effects of d_p and P over the entire MAPbBr₃ transmission window of interest, Figure 5e,f shows spectra modeled via Mie theory (dashed-dotted black/blue lines) as a function of d_p and P , respectively. In each case, the $l = 0.989$ MAPbBr₃ ceramic data (red line and shaded regions) and theoretical maximum transmission (dotted black lines) are provided for reference.

Figure 5d shows the effects of decreasing d_p from 305 to 35 nm in 40 nm increments with a fixed P of ~ 0.0002 . Transparency clearly increases across the window as d_p decreases, where the pore scattering effects are significantly stronger near the perovskite band edge compared to longer wavelengths. The data in Figure 5d assumes monodisperse d_p . However, in reality, d_p is polydisperse (see Figure 5c). We thus adapt our model to include the pore size distribution derived from NanoCT and track changes to the spectra as a function of P (see Figure S19 for a comparison of monodisperse vs polydisperse models). Figure 5f illustrates this data as a function of decreasing P between $0.0001 < P < 0.001$. The porosity that best matches the experimental data is ~ 0.0002 . Overall, the modeling makes it apparent that $P < 0.0001$ and $d_p < 100$ nm are ideal for optimal transparency in ~ 1 mm thick perovskite ceramics.

Unfortunately, eliminating the final few tenths or hundredths of a percent of residual porosity and controlling pore size to achieve near-optimal density ($\rho > 0.9999$) is no trivial task. Longer press times alone may not be practical to achieve “full” density since densification rates saturate as ρ approaches 0.99 (see Figure S20 and Table S2), giving diminishing transparency increases over extending pressing time frames. From a historical perspective, the development of near-full-density ceramics has required intimate knowledge and control of underlying sintering mechanism(s).^{56–62} There is currently a knowledge gap within the literature in this regard for halide perovskite materials, which needs to be closed in order to optimize their densities and thus transparency. This can be accomplished by classical uniaxial or isostatic pressing experiments that track densification kinetics through changes in the microstructural properties (e.g., ρ and $\langle d_g \rangle$) as a

Table 1. Comparison of Optical, Electrical, and Mechanical Properties of MAPbX₃ Ceramics and Single Crystals

sample	n @ 1 μm	k @ 1 μm	H (GPa)	E (GPa)*	μ_{H} ($\text{cm}^2 \text{V}^{-1} \text{s}^{-1}$)	resistivity ($\Omega\text{-cm}$)	N_{c} (cm^{-3})
MAPbBr ₃ crystal	2.05	1.0×10^{-6}	0.35 ± 0.01	18.67 ± 0.47	0.28	1.20×10^8	2.1×10^{11}
MAPbBr ₃ ceramic	2.04	2.9×10^{-5}	0.45 ± 0.03	17.32 ± 0.47	0.20	1.63×10^7	1.9×10^{12}
MAPbCl ₃ crystal	1.86	1.0×10^{-6}	0.33 ± 0.01	19.52 ± 0.11			
MAPbCl ₃ ceramic	1.87	2.7×10^{-5}	0.42 ± 0.04	18.17 ± 1.12			

*Estimated using a Poisson ratio of ~ 0.3 from prior work.⁶³

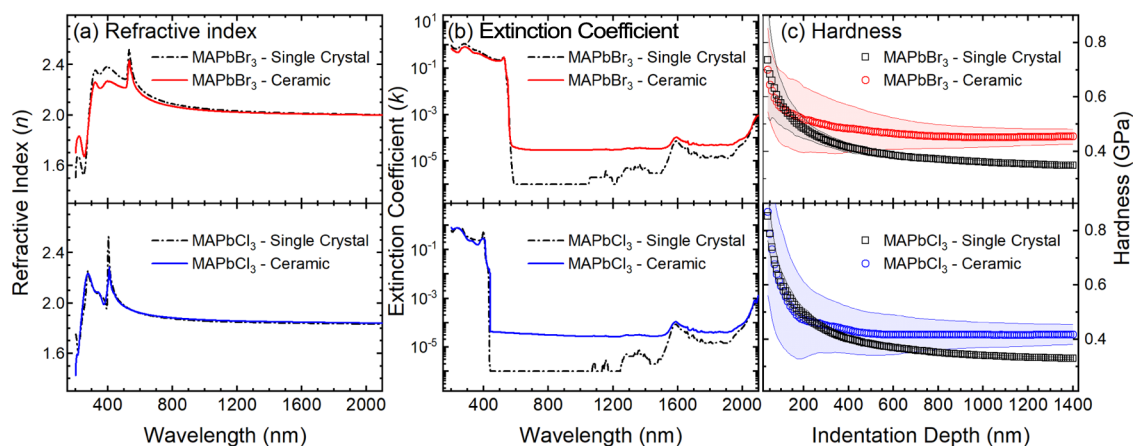


Figure 6. Comparison of optical and mechanical properties of MAPbBr₃ (top row) and MAPbCl₃ (bottom row) ceramics (colored solid lines/open circles) and single crystals (black dashed-dotted line/open squares). This includes refractive indices (a) and extinction coefficients (b) derived from spectroscopic ellipsometry as well as hardness (c) derived from nanoindentation. Shaded regions in (c) represent the standard deviation from 21 to 26 indentation measurements.

function of temperature, pressure, and starting powder grain size or purity. These kinetic measurements can be used to derive the rate-controlling sintering mechanism(s) as well as associated activation energies under various conditions. This underlying mechanistic knowledge can in turn be exploited to outline optimal starting powder properties as well as both green and white body pressing conditions to make ceramics with ideal properties for a given application and can additionally be used to produce high-quality polycrystalline ceramics with production times faster than those outlined here.

Comparison of Single Crystals and Transparent Polycrystalline Ceramics. Here, the optical (e.g., n and k), electrical (e.g., Hall mobility [m_{H}], resistivity, carrier concentration [N_{c}]), and mechanical properties (e.g., hardness [H] and Young's modulus [E]) of uniaxially pressed perovskite ceramics are benchmarked against solution-grown single-crystalline analogues. This is critical toward understanding the performance-manufacturability trade-off of polycrystalline ceramics versus single crystals. Table 1 summarizes material parameters derived from these experiments. First, Figure 6a,b plots n and k for MAPbX₃ ($X^- = \text{Br}^-, \text{Cl}^-$) ceramics (solid lines) and single crystals (dashed-dotted black lines). Ellipsometry methods/fitting procedure are outlined in a prior work⁵⁰ and dielectric functions for ceramics can be found in Figure S21. Effective ceramic n and k values slightly differ from those of their single-crystal analogues. This is expected due to the presence of pores causing enhanced scattering in the polycrystalline measurements, which reiterates the importance of continuing to develop methods to reduce ceramic porosity.

To assess the mechanical properties, nanoindentation was performed using a Berkovich tip pressed $\sim 1.5 \mu\text{m}$ into the perovskite at a strain rate of 0.2 s^{-1} (further details in the Materials and Methods section). Load–displacement curves for all measurements can be found in Figure S22. Hardness

(Figure 6c) and Young's modulus (Figure S23) plots were averaged (open circles or squares) from 21 to 26 indentations, where shaded regions represent measured standard deviation. Single-crystal and ceramic mechanical properties (see Table 1) are similar to each other and in line with prior MAPbX₃ work.^{11,19} Small deviations in H and E values are attributed to the preferred (001) orientation of the single crystals versus random orientation of grains within the polycrystalline ceramics (see XRD in Figure S2).¹¹ The soft nature of the perovskites alludes to plastic deformation playing an important role in the sintering mechanism of MAPbBr₃ and MAPbCl₃ as previously observed in MAPbI₃.¹⁹

Hall measurements demonstrate that MAPbBr₃ ceramics and single crystals are P-type with comparable mobilities, resistivity, and carrier densities (see Table 1). Electron mobilities are on the same order of magnitude as those of prior MAPbI₃ ceramics/single crystals (ca. $0.50\text{--}0.56 \text{ cm}^2 \text{V}^{-1} \text{s}^{-1}$).¹⁹ The general takeaway from these comparative measurements is that ceramics have properties that are similar to those of single crystals even with the known porosity issues discussed above. Thus, with further improvements in sintering conditions, polycrystalline ceramics can be viable candidates to replace single crystals in applications requiring large area, millimeter-thick active layers.

γ -ray Scintillation from Transparent Ceramics. Finally, we demonstrate γ -ray scintillation from transparent lead halide perovskite ceramics. Figure 7 shows a scintillation response from an $l = 1.134 \text{ mm}$ MAPbBr₃ (red line) ceramic when exposed to γ -ray irradiation with a ¹³⁷Cs source. Experimental details can be found in the Materials and Methods section. Notably, a clear excess of counts is observed on the photomultiplier tube (PMT) above the background (black and green lines) when the sample is irradiated with ¹³⁷Cs γ -rays. This is despite the MAPbBr₃ ceramic having a small

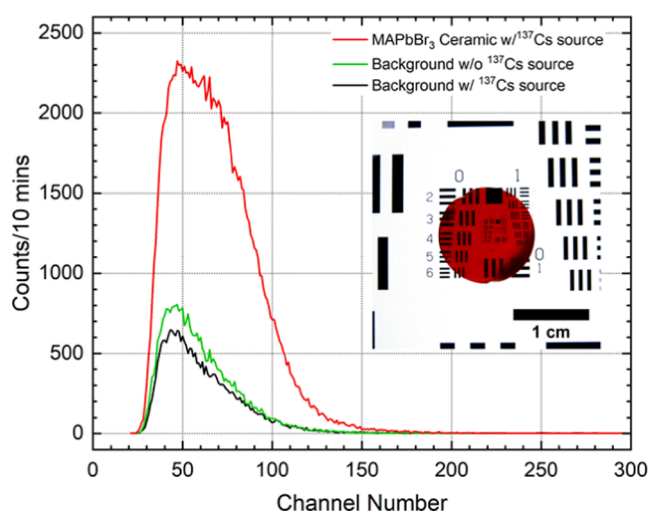


Figure 7. Scintillation from a MAPbBr₃ (red line; $l = 1.134$ mm) ceramic when exposed to γ -rays from a ¹³⁷Cs source. Background spectra of the bare PMT with the ¹³⁷Cs source on and no ceramic present (black) as well as with the ¹³⁷Cs source off but with the ceramic present (green) are provided as well. The inset shows an image of the MAPbBr₃ ceramic that was tested.

Stokes shift, nontrivial porosity, and poor overlap between MAPbBr₃ emission and the employed PMT's external quantum efficiency. Enhancing optical transparency, improving device architecture, and doping with active ions⁶⁴ (e.g., Mn²⁺) in order to increase the Stokes shift are all viable approaches to improve the scintillating response. Nonetheless, the proof-of-concept data in Figure 7 illustrate an interesting potential application space in which transparent polycrystalline perovskite ceramics could make an impact.

CONCLUSIONS

Overall, this work establishes nascent processing guidelines to produce freestanding, millimeter-thick optically transparent MAPbX₃ ceramics. It also provides the building blocks needed to eventually produce higher-density ($\rho > 0.9999$) perovskite ceramics with maximized optical transparency. While the focus here has been on MAPbBr₃ and MAPbCl₃, this methodology should be applicable to other room-temperature, cubic phase lead halide perovskites (e.g., FAPbBr₃, FAPbCl₃, FA/CsPbX₃, FA/MA/CsPbX₃, rare-earth doped lead halide perovskites, etc.).^{3,10,64} However, this will require meticulous control and an understanding of the processing methods from initial powder production to all stages of sintering/densification. Establishing this knowledge will permit the rapid production of ready-to-use halide perovskite ceramics with microstructures, optoelectronic properties, and physical dimensions that meet the performance criteria of specific applications.

MATERIALS AND METHODS

Materials. Lead(II) bromide (PbBr₂, $\geq 98\%$), lead(II) chloride (PbCl₂, $\geq 98\%$), N,N-dimethylformamide (DMF, 99.8% anhydrous), dimethylsulfoxide (DMSO, $\geq 99.9\%$ anhydrous), and hexane ($>95\%$ anhydrous) were purchased from Sigma-Aldrich. Methylammonium bromide (MABr, $>99.99\%$) and methylammonium chloride (MACl, $>99.99\%$) were purchased from GreatCell Solar Materials. MAX and PbX₂ (X = Br⁻, Cl⁻) salts were dried in a vacuum oven at ~ 50 °C for ~ 24 h prior to crystal growth. Solvents were used as received.

$\theta/2\theta$ X-ray Diffraction Measurements. $\theta/2\theta$ X-ray diffraction (XRD) measurements were made using a Rigaku SmartLab equipped

with a channel-cut Ge (220) double-bounce monochromator on the copper source side to strip the K α_2 and K β X-ray lines.

Thermogravimetric Analysis (TGA). TGA of the prepressed perovskite powders was carried out using a TA Q500. About 10–20 mg of each sample was loaded onto a platinum pan and heated at a ramp rate of 10 °C min⁻¹ to a final temperature of ~ 1000 °C in a nitrogen atmosphere.

Fabrication of Transparent Ceramics. MAPbBr₃ and MAPbCl₃ crystals were grown following a modified inverse temperature crystallization method from the literature.^{51,52} MAPbBr₃ and MAPbCl₃ crystals were then first ground with a mortar and pestle to form rough powders. The resulting powders were dried in a vacuum oven at ~ 50 °C for ~ 24 to ~ 48 h. This was followed by two subsequent pulverization steps with a Retsch PM200 Planetary ball mill with 50 mL zirconia jars and milling media. Pulverized and sieved powders were loaded into evacuable, cylindrical, stainless steel die sets (MSE or Chemplex) with diameters of 12.7 mm between two prepolished stainless steel spacers. Three stages of pressure were applied under dynamic vacuum at room temperature ($\sim 21 \pm 2$ °C) in a lab with ambient relative humidity in the range of $\sim 50 \pm 20\%$. First, two lower-pressure stages—35 MPa for ~ 1 h and 150 MPa for ~ 2 h, were used to produce an opaque green body ceramic (see Figure S5). Then, finishing stage-holding pressures between ~ 200 and 525 MPa were set for ca. 150–300 h. All ceramics were characterized thereafter without any additional annealing or polishing steps. Ceramics were stored under vacuum in the dark when not being characterized. Further details on all steps in the fabrication method can be found in the SI.

Scanning Electron Microscopy. Scanning electron microscopy (SEM) images were acquired using a Zeiss Gemini 500 scanning electron microscope equipped with an InLens detector for energy filtering and detection of low-voltage backscattered electrons. The microscope was operated at an accelerating voltage of 5 kV in order to prevent significant e-beam-induced damage during high-resolution imaging. Further details on $\langle d_g \rangle$ can be found in the SI.

Optical Profilometry. Surface roughness analysis was performed by using a Bruker ContourX-500 3D Optical Profilometer. Surface roughness measurements were acquired via phase shift interferometry using the 532 nm illumination source in order to achieve subangstrom resolution.

Transmission Measurements. Transmission spectra of all samples were acquired using a Cary 5000 UV–Vis–NIR spectrophotometer (Agilent Technologies) for wavelengths ranging from 300 to 3000 nm and a Nicolet iS50 FTIR spectrometer (ThermoFisher) for wavelengths longer than 3000 nm. Each sample was measured multiple times with a metal plate containing an ~ 4 mm aperture in the light path between the sample and the detector to limit forward scattering from being quantified as transmission.

Archimedes' Density Measurements. Archimedes' density measurements were performed using an Excellence XS Analytical Balance (Mettler Toledo, sensitivity down to ± 0.001 g cm⁻³). Anhydrous hexane was used for liquid mass measurements at temperatures of $\sim 21 \pm 2$ °C. Reported single-crystal densities represent the average from the values of five different MAPbBr₃ and MAPbCl₃ single crystals grown from solution. Averaged single-crystal densities (standard deviation provided) of 3.823 ± 0.031 g cm⁻³ (MAPbBr₃) and 3.115 ± 0.020 g cm⁻³ (MAPbCl₃) were used to derive the relative density values in Table S1.

X-ray 3D Nanotomography Methods. X-ray 3D tomographic imaging was performed using a Zeiss Xradia Ultra 810 NanoCT microscope, operating first in the large field of view mode (65 μ m field of view, starting with absorption contrast and then with Zernike phase contrast) followed by the high-resolution mode (16 μ m field of view, pixel resolution of 16 nm with nominal spatial resolution of 50 nm, absorption contrast only). Quasi-monochromatic X-rays were generated using a chromium source (~ 5.4 keV; ~ 2.3 Å), and X-rays were detected with a high-contrast scintillator-based detector and a corresponding optically coupled CCD detector. Zeiss XMReconstructor was used to build the tomography data into a 3D volume.

Pore analysis and figure preparation were performed using ORS Dragonfly. Further details can be found in the SI.

Light Scattering by Spherical Pores Modeling. Light scattering models were adapted from prior works. First, the scattering efficiency (Q_{sca}) was calculated for a range of pore sizes constrained by the NanoCT-derived pore size distribution (ca. 35–635 nm) for the $l = 0.989$ mm MAPbBr₃ ceramic (see Figure S15 and main text, Figure 5c). Specifically, Q_{sca} was calculated for pore diameters ranging from $d_p = 35$ nm to $d_p = 635$ nm in 10 nm steps. Pores were treated as spherical inclusions with refractive indices of $n = 1$ surrounded by a host medium with refractive indices taken from ellipsometry measurements on MAPbBr₃ single crystals. Q_{sca} was calculated via Mie theory using an established numerical approach (BHME scattering code, see Figure S16a). After calculating Q_{sca} , scattering cross sections (C_{sca}) for the entire pore distribution were calculated by multiplying the scattering efficiency by the projected area ($A_p = \pi d_p^2/4$) of the spherical pore such that ($C_{\text{sca}} = Q_{\text{sca}} \times A_p$, see Figure S16b). From there, the theoretical transmission of the sample was estimated via the Beer–Lambert extinction law. Further details are provided in the SI.

Variable Angle Spectroscopic Ellipsometry. Variable angle spectroscopic ellipsometry was carried out by using an RC2 ellipsometer (JA Woollam). Reflection measurements were collected from 50 to 80° at 5° increments for wavelengths 200–2500 nm. Optical dispersion data analysis of the raw ellipsometry data was performed using CompleteEASE v6.55 (JA Woollam).

Nanoindentation Methods. Nanoindentation was performed using a KLA Nano Indentor G200X equipped with an InForce 50 actuation head and a diamond Berkovich tip. Three separate 3 × 3 square indent arrays spaced 30 μm apart were collected at different locations on the sample with a target indentation depth of 1.5 μm and a constant strain rate of 0.2 s⁻¹. The continuous stiffness method (CSM) was employed for all measurements with a sinusoidal signal of ~2 nm in displacement magnitude at 110 Hz superimposed on the indentation load. Indentations on fused silica were performed before and after collections of each sample to monitor the integrity of the tip shape. Young's Modulus values were estimated using a Poisson's ratio of ~0.3.⁶³

Hall Measurements. Hall measurements were conducted by using a Lakeshore 8407 system in order to assess the mobility, resistivity, and carrier concentration of ceramics and single crystals. Emerging classes of photovoltaic and organic electronic materials are typically characterized by low mobilities that are difficult to measure. Thus, the Hall system must be operated in AC field mode, which has the ability to measure mobilities down to 0.001 cm² V⁻¹ s⁻¹. In this configuration, the field has a strength of 1.15T and is oscillated at a frequency of 100 mHz. The Hall samples were prepared using the standard Van der Pauw configuration and are allowed to stabilize for 1 min between each measurement. The sensitivity and AC gain settings are 200 μV and 48 dB, respectively. Multiple measurements were acquired and averaged to ensure good statistics.

γ-ray Scintillation Measurements. Radiation-induced luminescence measurements were measured by γ-ray irradiation using a 1 μCi ¹³⁷Cs source. The radioluminescence spectra were recorded by using a Hamamatsu R9800-100 super-bialkali photomultiplier tube (PMT) and a CAEN DT5730 500 MS/s 14-bit waveform digitizer. The PMT was biased at -1200 V for all measurements. Three spectra were recorded: bare PMT w/¹³⁷Cs source, MAPbBr₃ ceramic sample w/¹³⁷Cs source, and ceramic sample with no source. For each measurement, the photocathode, w/or w/o the ceramic sample present, was covered with 2 layers of PTFE tape (Mil-T-27730A). In order to prevent potential perovskite contamination, no optical coupling grease was used, which also contributes to suppression of light captured at the PMT due to the refractive index mismatches between perovskite–air–PMT boundaries.

■ ASSOCIATED CONTENT

Supporting Information

The Supporting Information is available free of charge at <https://pubs.acs.org/doi/10.1021/acsami.4c01517>.

3D, rotating view of irregularly shaped pores (AVI)

Materials; $\theta/2\theta$ XRD methods; TGA methods; crystal growth methods; ball milling details; uniaxial pressing details; SEM methods; optical profilometry methods; optical imaging methods; transmission measurement methods and simulations; Archimedes density measurement methods; X-ray nanotomography methods; pore modeling details, table of MAPbX₃ ceramics properties; transmission spectra of MAPbX₃ ceramics, single crystals, and simulations from 300 to 3000 nm; $\theta/2\theta$ XRD patterns of MAPbX₃ powders, single crystals, ceramics, and simulations; thermogravimetric analysis data; SEM images of MAPbX₃ powders; images of all MAPbX₃ and MAPbCl₃ ceramics; images of MAPbX₃ single crystals; transmission spectra of all MAPbX₃ ceramics; transmission of MAPbBr₃ ceramic 9 months after synthesis; ceramic transmission spectra from 0.3 to 25 μm; SEM sizing histograms for each ceramic; optical profilometry surface roughness maps of MAPbX₃ ceramics and corresponding polished stainless steel spacers; NanoCT data video and further SEM/tomography images of analyzed area, min and max Feret pore size histograms, scattering efficiencies, scattering cross sections, and extinction coefficients from pore modeling, transmission spectra from pore modeling, contour plots from modeling, comparison of polydisperse and monodisperse transmission spectra; experimental transmission spectra vs press time figure and table; dielectric functions of MAPbX₃ ceramics; loading curves from nanoindentation measurements; and estimated Young's modulus from nanoindentation measurements (PDF)

■ AUTHOR INFORMATION

Corresponding Authors

Michael C. Brennan – Air Force Research Laboratory, Materials and Manufacturing Directorate, Wright-Patterson Air Force Base, Ohio 45433, United States; Azimuth Corporation, Fairborn, Ohio 45342, United States; orcid.org/0000-0002-4482-5173; Email: michael.brennan.30.ctr@us.af.mil

Tod A. Grusenmeyer – Air Force Research Laboratory, Materials and Manufacturing Directorate, Wright-Patterson Air Force Base, Ohio 45433, United States; orcid.org/0000-0002-1842-056X; Email: tod.grusenmeyer.1@us.af.mil

Authors

Christopher L. McCleese – Air Force Research Laboratory, Materials and Manufacturing Directorate, Wright-Patterson Air Force Base, Ohio 45433, United States; Azimuth Corporation, Fairborn, Ohio 45342, United States; orcid.org/0000-0002-2114-8392

Lauren M. Loftus – Air Force Research Laboratory, Materials and Manufacturing Directorate, Wright-Patterson Air Force Base, Ohio 45433, United States; Azimuth Corporation,

Fairborn, Ohio 45342, United States; orcid.org/0000-0001-6829-3039

Jeremiah Lipp – Air Force Research Laboratory, Materials and Manufacturing Directorate, Wright-Patterson Air Force Base, Ohio 45433, United States; UES, Inc., Dayton, Ohio 45432, United States

Michael Febbraro – Department of Engineering Physics, Air Force Institute of Technology, Wright-Patterson Air Force Base, Ohio 45433, United States

Harris J. Hall – Air Force Research Laboratory, Sensors Directorate, Wright-Patterson Air Force Base, Ohio 45433, United States; orcid.org/0000-0003-4400-8656

David B. Turner – Air Force Research Laboratory, Materials and Manufacturing Directorate, Wright-Patterson Air Force Base, Ohio 45433, United States; Azimuth Corporation, Fairborn, Ohio 45342, United States; Air Force Research Laboratory, Sensors Directorate, Wright-Patterson Air Force Base, Ohio 45433, United States

Michael J. Carter – Air Force Research Laboratory, Materials and Manufacturing Directorate, Wright-Patterson Air Force Base, Ohio 45433, United States

Peter R. Stevenson – Air Force Research Laboratory, Materials and Manufacturing Directorate, Wright-Patterson Air Force Base, Ohio 45433, United States; orcid.org/0000-0003-3731-1630

Complete contact information is available at:
<https://pubs.acs.org/10.1021/acsami.4c01517>

Notes

The authors declare no competing financial interest.

ACKNOWLEDGMENTS

M.C.B., C.L.M., L.M.L., and T.A.G. acknowledge funding under AFRL/RXEP contract FA8650-22-D-5408. M.C.B. and T.A.G. acknowledge the support of Air Force Office of Scientific Research grant number 23RXCOR023. J.L. acknowledges funding under Air Force contract FA8659-18-C-5291. M.C.B. thanks Dr. Zachary Marsh for help with TGA measurements.

REFERENCES

- (1) Manser, J. S.; Christians, J. A.; Kamat, P. V. Intriguing Optoelectronic Properties of Metal Halide Perovskites. *Chem. Rev.* **2016**, *116*, 12956–13008.
- (2) Li, J.; Gu, Y.; Han, Z.; Liu, J.; Zou, Y.; Xu, X. Further Advancement of Perovskite Single Crystals. *J. Phys. Chem. Lett.* **2022**, *13*, 274–290.
- (3) Li, J.; Han, Z.; Yu, D.; Liu, J.; Hu, D.; Xu, X.; Zeng, H. Perovskite Single Crystals: Synthesis, Optoelectronic Properties, and Applications. *Adv. Funct. Mater.* **2021**, *31*, No. 2008684.
- (4) Jana, A.; Cho, S.; Patil, S. A.; Meena, A.; Jo, Y.; Sree, G. V.; Park, Y.; Kim, H.; Im, H.; Taylor, R. A. Perovskite: Scintillators, Direct Detectors, and X-ray Imagers. *Mater. Today* **2022**, *55*, 110–136.
- (5) Dey, A.; Ye, J.; De, A.; Debroye, E.; Ha, S. K.; Bladt, E.; Kshirsagar, A. S.; Wang, Z.; Yin, J.; Wang, Y.; et al. State of the Art and Prospects for Halide Perovskite Nanocrystals. *ACS Nano* **2021**, *15*, 10775–10981.
- (6) Kim, D.; Ryu, H.; Yeon Lim, S.; McCall, K. M.; Park, J.; Kim, S.; Kim, T. J.; Kim, J.; Soo Kim, Y.; Kanatzidis, M. G.; Cheong, H.; Jang, J. I. On the Origin of Room-Temperature Amplified Spontaneous Emission in CsPbBr₃ Single Crystals. *Chem. Mater.* **2021**, *33*, 7185–7193.
- (7) Luo, B.; Li, F.; Xu, F.; Xu, K.; Guo, Y.; Liu, Y.; Xia, Z.; Zhang, J. Z. B-Site Doped Lead Halide Perovskites: Synthesis, Engineering,

Photophysics, and Light Emission Applications. *J. Mater. Chem. C* **2019**, *7*, 2781–2808.

(8) Shen, W.; Chem, J.; Wu, J.; Li, X.; Zeng, H. Nonlinear Optics in Lead Halide Perovskites: Mechanisms and Applications. *ACS Photonics* **2021**, *8*, 113–124.

(9) Sun, Li.; Li, W.; Zhu, W.; Chen, Z. Single-Crystal Perovskite Detectors: Development and Perspectives. *J. Mater. Chem. C* **2020**, *8*, 11664.

(10) Yang, M.; Nie, Z.; Li, X.; Wang, R.; Zhao, Y.; Wang, H. Advances of Metal Halide Perovskite Large-Size Single Crystals in Photodetectors: From Crystal Materials to Growth Techniques. *J. Mater. Chem. C* **2023**, *11*, 5908–5967.

(11) Tu, Q.; Kim, D.; Shyikh, M.; Kanatzidis, M. G. Mechanics-Coupled Stability of Metal-Halide Perovskites. *Matter* **2021**, *4*, 2765–2809.

(12) Dai, Z.; Doyle, M. C.; Liu, X.; Hu, M.; Wang, Q.; Athanasiou, C. E.; Liu, Y.; Sheldon, B. W.; Gao, H.; Lie, S.; Padture, N. P. The Mechanical Behavior of Metal-Halide Perovskites: Elastically, Plasticity, Fracture, and Creep. *Scr. Mater.* **2023**, *223*, No. 115064.

(13) Goldstein, A.; Krell, A. Transparent Ceramics at 50: Progress Made and Further Prospects. *J. Am. Ceram. Soc.* **2016**, *99*, 3173–3197.

(14) Wang, S. F.; Zhang, J.; Luo, D. W.; Gu, F.; Tang, D. Y.; Dong, Z. L.; Tan, G. E. B.; Que, W. X.; Zhang, T. S.; Li, S.; Kong, L. B. Transparent Ceramics: Processing, Materials, and Applications. *Prog. Solid State Chem.* **2013**, *41*, 20–54.

(15) Krell, A.; Hutzler, T.; Klimke, J. Transmission Physics and Consequences for Materials Selection, Manufacturing, and Applications. *J. Euro. Ceram. Soc.* **2009**, *29*, 207–221.

(16) Johnson, R.; Biswas, P.; Ramavath, P.; Kumar, R. S.; Padmanabham. Transparent Polycrystalline Ceramics: An Overview. *Trans. Indian Ceram. Soc.* **2012**, *71*, 73–85.

(17) Suárez, M.; Fernández, A.; Torrecillas, R.; Menendez, J. L. *Sintering to Transparency of Polycrystalline Ceramic Materials*; InTech, 2012.

(18) Skrotzki, W.; Frommeyer, O.; Haasen, P. Plasticity of Polycrystalline Ionic Solids. *Phys. Status Solidi A* **1981**, *66*, 219–228.

(19) Shrestha, S.; et al. High-Performance Direct Conversion of X-Ray Detectors Based on Sintered Hybrid Lead Triiodide Perovskite Wafers. *Nat. Photonics* **2017**, *11*, 436–441.

(20) Deumel, S.; van Breemen, A.; Gelinck, G.; et al. High-Sensitivity High-Resolution X-ray Imaging with Soft-Sintered Metal Halide Perovskites. *Nat. Electronics* **2021**, *4*, 681–688.

(21) Tu, Q.; Kim, D.; Shyikh, M.; Kanatzidis, M. G. Mechanics-Coupled Stability of Metal-Halide Perovskites. *Matter* **2021**, *4*, 2765–2809.

(22) Yakunin, S.; Sytnyk, M.; Kriegner, D.; Shrestha, S.; Richter, M.; Matt, G. J.; Azimi, H.; Brabec, C. J.; Stangl, J.; Kovalenko, M. V.; Heiss, W. Detection of X-Ray Photons by Solution-Processed Lead Halide Perovskites. *Nat. Photonics* **2015**, *9*, 444–449.

(23) Sakhatskyi, K.; Turedi, B.; Matt, G. J.; Wu, E.; Sakhatska, A.; Bartosh, V.; Lintangpradipto, M. N.; Naphade, R.; Sorubalko, I.; Mohammed, O. F.; Yakunin, S.; Bakr, O. M.; Kovalenko, M. V. Stable Perovskite Single Crystal X-Ray Imaging Detectors with Single-Photon Sensitivity. *Nat. Photon* **2023**, *17*, 510–517.

(24) Witt, C.; Schmid, A.; Leupold, N.; Schultz, M.; Höcker, J.; Baumann, A.; Moos, R.; Panzer, F. Impact of Pressure and Temperature on the Compactions Dynamics and Layer Properties of Powder-Pressed Methylammonium Lead Halide Thick Films. *ACS Appl. Electron. Mater.* **2020**, *2*, 2619–2628.

(25) Hu, M.; Jia, S.; Liu, Y.; Cui, J.; Zhang, Y.; Su, H.; Cao, S.; Mo, L.; Chu, D.; Zhao, G.; Zhao, K.; Yang, Z.; Liu, S. F. Large and Dense Organic-Inorganic Hybrid Perovskite CH₃NH₃PbI₃ Wafer Fabrication by One-Step Reactive Direct Wafer Production with High X-Ray Sensitivity. *ACS Appl. Mater. Interfaces* **2020**, *12*, 16592–16600.

(26) Zheng, L.; Nozariasbmarz, A.; Hou, Y.; Yoon, J.; Li, W.; Zhang, Y.; Wu, H.; Yang, D.; Ye, T.; Sanghadasa, M.; Wang, K.; Poudel, P.; Priya, S.; Wang, K. A Universal All-Solid Synthesis for

High throughput Production of Halide Perovskites. *Nature. Commun.* **2022**, *13*, 7399.

(27) Yu, J.; Qu, Y.; Deng, Y.; Men, D.; Tian, N.; Li, L.; Zheng, J.; Huang, Y.; Luo, Y.; Tan, W. Hot-Pressed $\text{CH}_3\text{NH}_3\text{PbI}_3$ Polycrystalline Wafers for Near-Infrared Bioimaging and Medical X-Ray Imaging. *J. Mater. Chem. C* **2023**, *11*, 5815–5824.

(28) Borri, C.; Calisi, N.; Galvanetto, E.; Falsini, N.; Biccari, F.; Vinattieri, A.; Cucinotta, G.; Caporali, S. First Proof-of-Principle of Inorganic Lead Halide Perovskites Deposition by Magnetron Sputtering. *Nanomaterials* **2020**, *10*, 60.

(29) Noculak, A.; Boehme, S. C.; Aebli, M.; Shynkarenko, Y.; McCall, K. M.; Kovalenko, M. V. Pressure-Induced Perovskite-to-non-Perovskite Phase Transition in CsPbBr_3 . *Helv. Chim. Acta* **2021**, *104*, No. e2000222.

(30) Kiyek, V. M.; Birkhölzer, Y. A.; Smirnov, Y.; Ledinsky, M.; Remes, Z.; Momand, J.; Kooi, B. J.; Koster, G.; Rijnders, G.; Morales-Masis, M. Single Source, Solvent-Free, Room Temperature Deposition of Black $\gamma\text{-CsSnI}_3$ Films. *Adv. Mater. Interfaces* **2020**, *7*, No. 2000162.

(31) Hong, Z.; Tan, D.; John, R. A.; Tay, Y. K. E.; Ho, Y. K. T.; Zhao, X.; Sum, T. C.; Mathew, N.; Garcia, F.; Soo, H. S. Completely Solvent-Free Protocols to Access Phase-Pure, Metastable Metal Halide Perovskites and Functional Photodetectors from the Precursor Salts. *iScience* **2019**, *16*, 312–325.

(32) Yang, B.; Pan, W.; Wu, H.; Niu, H.; Yuan, J. H.; Xue, K. H.; Yin, L.; Du, X.; Miao, X. S.; Yang, X.; Xie, Q.; Tang, J. Heteroepitaxial Passivation of $\text{Cs}_2\text{AgBiBr}_6$ Wafers with Suppressed Ionic Migration for X-Ray Imaging. *Nat. Commun.* **2019**, *10*, No. 1989.

(33) Tie, S.; Zhao, W.; Xin, D.; Zhang, M.; Long, J.; Chen, Q.; Zheng, X.; Zhu, J.; Zhang, W. H. Robust Fabrication of Hybrid Lead-Free Perovskite Pellets for Stable X-Ray Detectors with Low Detection Limit. *Adv. Mater.* **2020**, *32*, No. 2001981.

(34) Han, K.; Sakhatskiy, K.; Jin, J.; Zhang, Q.; Kovalenko, M. V.; Xia, Z. Seed-Crystal-Induced Cold Sintering Toward Metal Halide Transparent Ceramic Scintillators. *Adv. Mater.* **2022**, *34*, No. 2110420.

(35) Matsushima, T.; Fijihara, T.; Qin, C.; Terakawa, S.; Esaki, Y.; Hwang, S.; Sandanayaka, A. S. D.; Potsavage, W. J.; Adachi, C. Morphological Control of Organic-Inorganic Perovskite Layers by Hot Isostatic Pressing for Efficient Planar Solar Cells. *J. Mater. Chem. A* **2015**, *3*, 17780.

(36) Xiao, J.; Yang, Y.; Xu, X.; Shi, J.; Zhu, L.; Lv, S.; Wu, H.; Luo, Y.; Li, D.; Meng, Q. Pressure-Assisted $\text{CH}_3\text{NH}_3\text{PbI}_3$ Morphology Reconstruction to Improve the High Performance of Perovskite Solar Cell. *J. Mater. Chem. A* **2015**, *3*, 5289.

(37) Yu, J.; Wang, M.; Lin, S. Probing the Soft and Nanoductile Mechanical Nature of Single and Polycrystalline Organic-Inorganic Hybrid Perovskites for Flexible Functional Devices. *ACS Nano* **2016**, *10*, 11044–11057.

(38) Peelen, J. G. J.; Metselaar, R. Light Scattering by Pores in Polycrystalline Materials: Transmission Properties of Alumina. *J. Appl. Phys.* **1974**, *45*, 216.

(39) Apetz, R.; Van Bruggen, M. P. B. Transparent alumina: A Light Scattering Model. *J. Am. Ceram. Soc.* **2003**, *86*, 480–486.

(40) Hříbalová, S.; Pabst, W. Modeling Light Scattering by Spherical Pores for calculating the Transmittance of Transparent Ceramics – All You Need to Know. *J. Euro. Ceram. Soc.* **2021**, *41*, 2169–2192.

(41) Krell, A.; Blank, P.; Ma, H.; Hutzler, T.; Van Bruggen, M. P. B.; van Bruggen, M. P. B.; Apetz, R. Transparent Sintered Corundum with High Hardness and Strength. *J. Am. Ceram. Soc.* **2003**, *86*, 12–18.

(42) Furuse, H.; Horiuchi, N.; Kim, B. N. Transparent Non-Cubic Laser Ceramics with Fine Microstructure. *Sci. Rep.* **2019**, *9*, No. 10300.

(43) Furuse, H.; Okabe, T.; Shirato, H.; Kato, D.; Horiuchi, Morita, K.; Kim, B. N. High-Optical-Quality Non-Cubic Yb^{3+} -doped $\text{Ca}_{10}(\text{PO}_4)_6\text{F}_2$ (Yb:FAP) Laser Ceramics. *Opt. Mater. Express* **2021**, *11*, 1756–1762.

(44) Shahbazi, H.; Tataei, M.; Enayati, M. H.; Shafeiey, A.; Azizi Malekabadi, M. Structure-Transmission Relationship in Transparent Ceramics. *J. Alloys Compd.* **2019**, *785*, 260–285.

(45) Ishteev, A.; Konstantinova, K.; Ermolaev, G.; Kiselev, D.; Muratov, D.; Voronova, M.; Ilina, T.; Lagov, P.; Uvarov, O.; Pavlov, Y.; Letovaltseva, M.; Arsenin, A.; Volkov, V.; Didenko, S.; Saranin, D.; Di Carlo, A. Investigation of Structural and Optical Properties of MAPbBr_3 Monocrystals under Fast Electron Irradiation. *J. Mater. Chem. C* **2022**, *10*, 5821–5828.

(46) He, C.; Zha, G.; Deng, C.; An, Y.; Mao, R.; Liu, Y.; Lu, Y.; Chen, Z. Refractive Index Dispersion of Organic-Inorganic Hybrid Halide Perovskite $\text{CH}_3\text{NH}_3\text{PbX}_3$ ($X = \text{Cl}, \text{Br}, \text{I}$) Single Crystal. *Cryst. Res. Technol.* **2019**, *54*, No. 1900011.

(47) Handa, T.; Tahara, H.; Aharen, T.; Kanemitsu, Y. Large Negative Thermo-Optic Coefficients of Halide Perovskites. *Sci. Adv.* **2019**, *5*, No. eaax0786.

(48) Sabatini, R. P.; Liao, C.; Bernardi, S.; Mao, W.; Rahme, M. S.; Widmer-Cooper, A.; Bach, U.; Huang, S.; Ho-Baillie, A. W. Y.; Lakhwani, G. Solution-Processed Faraday Rotators Using Single Crystal Lead Halide Perovskites. *Adv. Sci.* **2020**, *7*, No. 1902950.

(49) Leguy, A. M. A.; Azarhoosh, P.; Alonso, M. I.; Campoy-Quiles, M.; Compoy-Quiles, M.; Weber, O. J.; Yao, J.; Bryant, D.; Weller, M. T.; Nelson, J.; Neslon, J.; Walsh, A.; van Schilfgaarde, M.; van Schilfgaarde, M.; Barnes, P. R. F. Experimental and Theoretical Optical Properties of Methylammonium Lead Halide Perovskites. *Nanoscale* **2016**, *8*, 6317.

(50) McCleese, C. L.; Brennan, M. C.; Episcopo, N.; Sun, L.; Hong, N.; Ramana, C.; Grusenmeyer, T. A.; Stevenson, R. P. Optical Dispersion Data Analysis of Single Crystal $\text{CH}_3\text{NH}_3\text{PbBr}_3$ for Optimized Perovskite Solar Cell Active Layer Absorptance. *ChemRxiv. Cambridge: Cambridge Open Engage. Materials Science*, November 27th 2023 (Accessed Dec 20, 2023).

(51) Saidaminov, M. I.; Abdellhady, A. L.; Murali, B.; Alarousu, E.; Burlakov, V. M.; Peng, W. L.; Dursun, I.; Wang, L.; He, Y.; Maculan, G.; Goriely, A.; Wu, T.; Mohammed, O. F.; Bakr, O. M. High-Quality Bulk Hybrid Perovskite Single Crystals within Minutes by Inverse Temperature Crystallization. *Nat. Commun.* **2015**, *6*, No. 7586.

(52) Nandi, P.; Giri, C.; Swain, D.; Manju, U.; Topwal, D. Room Temperature Growth of $\text{CH}_3\text{NH}_3\text{PbCl}_3$ Single Crystals by Solvent Evaporation Method. *CrystEngCommun* **2019**, *21*, 656.

(53) Nagabhushana, G. P.; Shivaramaiah, R.; Navrotsky, A. Direct Calorimetric Verification of Thermodynamic Instability of Lead Halide Hybrid Perovskites. *Proc. Natl. Acad. Sci. U.S.A.* **2016**, *113*, 7717–7721.

(54) Stuer, M.; Bowen, P.; Cantoni, M.; Pecharroman, C.; Zhao, Z. Nanopore Characterization and Optical Modeling of Transparent Polycrystalline Alumina. *Adv. Funct. Mater.* **2012**, *22*, 2303–2309.

(55) Bohren, C. F.; Huffman, D. R. *Absorption and Scattering of Light by Small Particles*; Wiley-Interscience, New York, 1983.

(56) Rahaman, N. M. *Sintering of Ceramics*, 2nd ed., CRC Press Taylor and Francis, Boca Raton FL, USA, 2008.

(57) Coble, R. L. Diffusion Models for Hot Pressing with Surface Energy and Pressure Effects as Driving Forces. *J. Appl. Phys.* **1970**, *41*, 4798.

(58) Coble, R. L. *Mechanisms of Densification during Hot Press, in Sintering Related Phenomena*; Kuczynski, G. C.; Hooton, N. A.; Gibbons, C. F., Eds.; Gordon and Brek: New York, 1967; p 329.

(59) Wang, J.; Raj, R. Estimate of Activation Energies for Boundary Diffusion from Rate-Controlled Sintering of Pure Alumina Doped with Zirconia. *J. Am. Ceram. Soc.* **1990**, *73*, 1172–1175.

(60) Du, X.; Zhang, Z.; Wang, Y.; Wang, J.; Wang, W.; Wang, H.; Fu, Z. Hot-Pressing Kinetics and Densification Mechanisms of Boron Carbide. *J. Am. Ceram. Soc.* **2015**, *98*, 1400–1406.

(61) Kang, S.-J. L.; Yang, Y.-I. Sintering Kinetics at the Final Stage Sintering: Model Calculation and Map Construction. *Acta Mater.* **2004**, *52*, 4573–4578.

(62) Bernard-Granger, G.; Guizard, C. Apparent Activation Energy for Densification of a Commercially Available Granulated Zirconia Powder. *J. Am. Ceram. Soc.* **2007**, *90*, 1246–1250.

(63) Faghihnasiri, M.; Izadifard, M.; Ebrahim Ghazi, M. DFT Study of Mechanical Properties and Stability of Cubic Methylammonium Lead Halide Perovskites ($\text{CH}_3\text{NH}_3\text{PbX}_3$, X = I, Br, Cl). *J. Phys. Chem. C* **2017**, *121*, 27059–27070.

(64) Nazarenko, O.; Yakunin, S.; Morad, V.; Cherniukh, I.; Kovalenko, M. V. Single Crystals of Caesium Formamidinium Lead Halide Perovskite: Solution Growth and Gamma Dosimetry. *NPG Asia Mater.* **2017**, *9*, No. e373.